

A Systematic Relationship between Intraseasonal Variability and Mean State Bias
in AGCM Simulations

Daehyun Kim¹, Adam H. Sobel², Eric D. Maloney³,
Dargan M. W. Frierson⁴, and In-Sik Kang⁵

¹*Lamont-Doherty Earth Observatory, Columbia University, Palisades, New York*

²*Department of Applied Physics and Applied Mathematics, and Department of Earth and
Environmental Sciences, Columbia University, New York, New York*

³*Department of Atmospheric Science, Colorado State University, Fort Collins, Colorado*

⁴*Department of Atmospheric Sciences, University of Washington, Seattle, Washington*

⁵*School of Earth and Environmental Sciences, Seoul National University, Seoul, South Korea*

October 2010

to be submitted to Journal of Climate

*Corresponding author address: Daehyun Kim, Lamont-Doherty Earth Observatory,
Columbia University, Palisades, New York. E-mail: dkim@ldeo.columbia.edu

Abstract

Systematic relationships between aspects of intraseasonal variability (ISV) and mean state bias are shown in a number of atmospheric general circulation model (AGCM) simulations. When AGCMs are categorized as either strong-ISV or weak-ISV models, it is shown that seasonal mean precipitation patterns are similar among models in the same group, but are significantly different from those of the other group. Strong-ISV models simulate excessive rainfall over the south Asian summer monsoon and the northwest Pacific monsoon regions during boreal summer. Larger ISV amplitude also corresponds closely to a larger ratio of eastward- to westward-propagating variance, but no model matches observations in both quantities simultaneously; a realistic eastward/westward ratio is simulated only when variance exceeds that observed. Three sets of paired simulations, in which only one parameter in the convection scheme is changed to enhance the moisture sensitivity of convection, are used to explore common differences between the two groups in greater detail. In strong-ISV models, the mean and the standard deviation of surface latent heat flux is greater, convective rain fraction is smaller, and tropical tropospheric temperatures are smaller compared to weak-ISV models. The instantaneous joint relationships between relative humidity and precipitation differ in some respects when strong- and weak-ISV models are compared, these differences are not systematic enough to explain the differences in ISV amplitude. On the other hand, there are systematic differences in the frequency with which specific values of

humidity and precipitation occur. In strong-ISV models, columns with higher saturation fraction and rain rate occur more frequently and make a greater contribution to total precipitation.

1. Introduction

It is well known that over the tropics, there is significant variability of rainfall fluctuating with time scales shorter than a season, known as intraseasonal variability (ISV). The dominant mode of tropical ISV is the Madden-Julian oscillation (MJO, Madden and Julian 1971; Madden and Julian 1972), characterized by its planetary spatial scale of wavenumber 1-3, low-frequency period of 30-60 days, as well as its prominent eastward propagation over the whole globe. As they modulate deep convection over the tropics, the MJO has large impacts on a wide variety of climate phenomena across different spatial and temporal scales. Some examples include the onset and break of the Indian and Australian summer monsoons (e.g. Yasunari 1979; Wheeler and McBride 2005), the formation of tropical cyclones (e.g. Liebmann et al. 1994; Maloney and Hartmann 2000a; Maloney and Hartmann 2000b; Bessafi and Wheeler 2006) and the onset of some El Nino events (e.g. Takayabu et al. 1999; Bergman et al. 2001; Kessler 2001).

Simulation of ISV, including the MJO, however, has been a difficult test for most climate models, from the Atmospheric Model Intercomparison Project (AMIP, Slingo et al. 1996) to the recent Coupled Model Intercomparison Project-3 (CMIP3, Lin et al. 2006). Lin et al. (2006) showed that only 2 models in CMIP3 had MJO variance comparable to observations, with even those lacking realism in many other MJO features.

At the same time, however, many previous studies have shown that simulation of the MJO can be improved by changing aspects of the cumulus parameterization of the GCM. The methods suggested include employing inhibition mechanisms associated with cumulus convection (Tokioka et al. 1988; Wang and Schlesinger 1999; Maloney and Hartmann 2001; Lee et al. 2003; Zhang and Mu 2005; Lin et al. 2008), an improved representation of downdrafts and rain re-evaporation (Maloney and Hartmann 2001), and modified convective closures (Zhang and Mu 2005).

When we change a given model to improve one aspect of the climate simulation, usually it produces changes in other aspects also, because of complex interactions among model components. Wang and Schlesinger (1999) and Slingo et al. (1996) documented relationships between the strength of ISV and the mean state in uncoupled atmospheric general circulation models. Slingo et al. (1996) showed that mean precipitation tends to be more confined to high sea surface temperature (SST) regions in models which simulate stronger ISV. Similarly, Wang and Schlesinger (1999) suggested, using various versions of one AGCM, that a strong relationship between precipitation and SST is necessary to properly simulate ISV. Because the above studies focused on the boreal winter season, they found that mean precipitation is more confined to the south Pacific convergence zone (SPCZ) region when a model simulates strong ISV.

In general, climate models are developed for the primary purpose of simulating

climate variability and change on time scales from interannual to decadal and longer, including projections of long-term change due to greenhouse gas forcing. It follows that features of the climate in long-term averages are perceived as more important than intraseasonal variability. We document here something which we suspect is known to many modeling groups, and which may be the reason for poor MJO simulation in many models: it is difficult to improve MJO simulation without degrading the mean state simulation, because of a systematic relationship between them. We show that there is a systematic relationship between the strength of ISV and boreal summer and winter mean bias in 10 AGCM simulations.

Section 2 describes the participating models and the data used for validation. The relationship between simulations of the ISV and the mean state from 10 different AGCM simulations is shown in section 3. A diagnostic analysis is used to find common differences between strong ISV and weak ISV models in later part of section 3. Summary and conclusions are given in section 4.

2. Participating Models and Data

a. Participating Models

Ten different climate simulations from 5 different atmospheric GCMs (AGCMs) are used in this study. Table 1 summarizes the model configurations and simulation details, including the convection scheme used in each model, the horizontal and vertical resolution, and the simulation period. All simulations are integrated for at

least 10 years. All 10 simulations are used in the first part of the next section, to show the general relationship between ISV and the mean state. Then we concentrate on three pairs of simulations with AM2, SNU, and CAM3.1R, in which the same configurations are used except for one parameter in the cumulus parameterization. The Tokioka modification (Tokioka et al. 1988), which suppresses convective plumes with entrainment rates less than a threshold that varies inversely with planetary boundary layer (PBL) depth, is implemented in AM2 and SNU with different threshold values. In that modification, threshold value is defined as $\mu_{\min} = \alpha/D$, where D is the depth of the planetary boundary layer (PBL) and alpha is a non-negative constant. The constant alpha, which determines the strength of triggering, is set to 0.025 and 0.1 in two different versions of AM2, while 0 and 0.1 are used in SNU models. Rain re-evaporation efficiency is modified in CAM3.1R from 0.05 to 0.6 in a model that also has a Tokioka-like minimum entrainment threshold of 0.0001 m^{-1} (which would correspond to $\alpha=0.1$ for a PBL depth of 1 km) employed. Hannah and Maloney (2010) demonstrated the sensitivity of ISV in this model to minimum entrainment threshold. The modifications have been shown to improve the ISV simulation in each model (Lin et al. 2008; Sobel et al. 2010). Considerable analysis of the simulated MJO dynamics has been performed for each of these three models, including sensitivity to the convective parameters described above [e.g., Maloney and Sobel (2004) and Maloney et al. (2010) for CAM3.1R; Sobel et al. (2010) for AM2; Lee et al. (2003) and Lin et al. (2008) for SNU).

b. Observational Data

We validate the simulations of rainfall against the Global Precipitation Climatology Project (GPCP, Huffman et al. 2001) product version 1.1. The tropospheric zonal winds and temperature are from the National Center for Environmental Prediction/National Center for Atmospheric Research (NCEP/NCAR) reanalysis data (Kalnay et al. 1996) and the interim reanalysis from European Centre for Medium-Range Weather Forecasts (Simmons et al. 2007). The Special Sensor Microwave/Imager (SSM/I) - Tropical Rainfall Measuring Mission (TRMM) Microwave Imager (TMI) combined precipitable water data is also used.

3. Results

a. Results from 10 simulations with 6 models

Figure 1 shows the all-season standard deviation of 20-100 day bandpass filtered precipitation. It is clear from this figure that stronger ISV of precipitation is observed in simulations in the right column than those in the left column. Based on Figure 1, we cluster simulations into two groups; strong-ISV (right column) and weak-ISV (left column) models. The separation is clear in terms of area averaged standard deviation over the tropics in Figure 3. The increased variance does not necessarily translate into more realism, however. All simulations in the right column overestimate the amplitude of ISV, as measured by the variance, to varying extents.

A significant difference between the two groups is also found in the propagation direction of ISV. Figure 2 shows lag correlation of 10°S - 10°N averaged 20-100 day bandpass filtered 850hPa zonal wind against a reference point in the equatorial Indian Ocean ($75\text{-}90^{\circ}\text{E}$, 5°S - 5°N). The intraseasonal anomalies of zonal wind propagate from west to east through the Indian Ocean in the two different reanalysis products (Figures 2a and 2g). The eastward propagating feature is well known as one of the basic characteristics of the MJO. The weak-ISV models exhibit near standing or westward propagation, opposite to what is observed. The strong-ISV models simulate eastward propagation better than the weak-ISV models. In AM2, SNU, and CAM3.1R, modifications to the convection scheme to enhance the moisture sensitivity of convection result in an improvement of the eastward propagation, as reported in previous studies (Tokioka et al. 1988; Wang and Schlesinger 1999; Lin et al. 2008; Sobel et al. 2010).

In Figure 3, the relationship between the strength of ISV and the dominant propagation direction of ISV is summarized in a scatter diagram. The strength metric is obtained by averaging the standard deviation of 20-100 day filtered precipitation over the tropics (30°S - 30°N , $0\text{-}360^{\circ}\text{E}$). For the propagation direction metric, the eastward/westward ratio of ISV is calculated from space-time power spectra, by dividing the sum of the spectral power over eastward-propagating zonal wavenumbers 1-3 and frequency range 30-70 days by its westward-propagating counterpart. Figure 3 shows that there is an approximate linear relationship between

the two metrics. Overall, weak-ISV models (open circles) underestimate the eastward/westward ratio metric compared to observations, although they reasonably simulate the magnitude of ISV. Note that all weak-ISV models have smaller ISV magnitude than strong-ISV models. Strong-ISV models generally show east/west ratios comparable to that of observations and larger than those of the weak-ISV models (except for GEOS5). We find striking the extent to which the relationship plotted for the models is compact and linear, while simultaneously the observations deviate from it. There is no model which simultaneously simulates the observed variance and eastward/westward ratio. Models with an eastward/westward ratio comparable to that observed overestimate the variance. Apparently even if we are willing to accept significant degradation in the simulation of the mean state (as is shown below to occur in the strong-ISV model) we are not yet able to produce a fully realistic MJO simulation.

To investigate the relationship between ISV characteristics and the mean state, May-October averaged precipitation is shown in Figure 4. In the western Hemisphere, observed boreal summer mean precipitation is characterized by maxima in several locations, including the equatorial Indian Ocean, the northwest Pacific, west of the India and Indochina peninsula, west of the Philippines, and east of Papua New Guinea (Figure 4). While most of these observed maxima are captured in most simulations - with different fidelities - there are similarities in the precipitation patterns within strong- and weak-ISV model groups. For example, in

weak-ISV models, precipitation maxima over the central Pacific are prominent with a compensating dry bias over the west Pacific. In 4 out of 5 strong-ISV models, a zonally elongated precipitation pattern is simulated from 60°E to 160°E and between 10°N to 20°N (excepting AM2). This is clearly distinguished from the intertropical convergence zone (ITCZ) which extends from 160°E to the western boundary of the American continent at about 5°N.

When we focus on the west Pacific (WP, 120-160°E, 5°S-15°N) and equatorial Indian Ocean (IO, 60-95°E, 15°S-5°N) regions, we find a clear difference between the strong- and weak-ISV groups. Weak-ISV models simulate stronger (weaker) precipitation in the IO (WP) than the strong-ISV models in the right column. Compared to observations, the weak-ISV models generally have a wet (dry) bias over the IO (WP) region, while the signs of the biases are reversed in the right column. Although mean precipitation is generally higher over the IO region for the weak-ISV models, the sub-seasonal variability of precipitation is stronger there in the strong-ISV models. This implies that the increase of sub-seasonal variability is not a result of higher mean rainfall in this region. A systematic difference between strong- and weak-ISV models groups is also observed during boreal winter. There is a tendency in strong-ISV models for precipitation in the SPCZ (south Pacific convergence zone) to be stronger while rainfall in the eastern Pacific ITCZ is weaker than in weak-ISV models (Figure 5).

Figure 6 summarizes the relationship between ISV and mean state simulation in a scatter diagram. The transverse axis in Figure 6 is the ISV strength metric used in Figure 3. The ordinate axis is a May-October and November-April mean precipitation index, respectively, defined as the mean precipitation difference between the WP and IO regions (see caption). It is shown in Figure 6 that a model with stronger ISV tends to simulate a larger difference of mean precipitation between the selected regions in both seasons, with even more precipitation occurring over the wetter WP warm pool. A linear relationship between ISV strength and mean precipitation index in Figure 6 demonstrates that there is a systematic relationship between ISV characteristics and mean state bias simulated in 10 different AGCM simulations. Strengthening the magnitude of ISV and improving the propagation direction of ISV result in a degradation of the mean state at least by this metric (an increase of the difference of the mean precipitation index from its observed value).

b. Detailed analysis of three model pairs

We next conduct a more detailed search for common features that distinguish strong-ISV models from weak-ISV models using three sets of paired simulations with AM2, SNU, and CAM3.1R.

Luo and Stephens (2006) examined the excessive boreal summer mean precipitation over the west Pacific in SPCAM. They suggested an anomalously

strong convection-wind-evaporation feedback, partly caused by the 2-dimensional geometry of the cloud resolving model implemented in SPCAM, was the cause of the precipitation bias. We also find that evaporation is larger in the strong-ISV models than in the weak-ISV models. Figure 7 shows a difference map (strong-ISV version minus weak-ISV version) of May-October precipitation and evaporation in each pair of simulation. There is an enhancement of surface latent heat flux in the regions where precipitation is increased (Fig. 7). Furthermore, the increase of mean latent heat flux is accompanied by an increase in variance at sub-seasonal time-scales (Fig. 8). Therefore, the argument about too-strong convection-wind-evaporation by Luo and Stephens is consistent with our results. However, the additional reasoning that the cloud resolving model geometry causes the excessive feedback is not supported by the results here, because a similar bias appears in models with conventional parameterizations. Our results demonstrate that the problem is not a specific one for models with cloud resolving models embedded in each large-scale grid box, but rather is a common symptom of models that overestimate the strength of ISV. Some of the excessive strength of this feedback is likely due to the fixed SST lower boundary. Models run over a dynamic ocean or a slab ocean will have reduced amplitude of this feedback, since the increased latent heat flux would result in a cooling of the ocean surface, and suppression of convection.

The fraction of rainfall produced by the convection scheme (as opposed to grid-scale saturation) is expected to be smaller in a strong-ISV model compared to a

weak-ISV one if the minimum entrainment rate threshold or the rain re-evaporation efficiency has been increased in the former relative to the latter. This expectation is borne out by figure 9, which shows difference maps (strong-ISV minus weak-ISV) of the annual mean convective rain fraction for the three model pairs. In Figure 9, AM2 has convective rain fraction reduced more than 50 percent over the west Pacific region, where mean precipitation increases significantly. SNU and CAM3.1R also show an overall reduction of convective rainfall fraction over the tropics.

Figure 10 shows a scatter plot of the standard deviation of intraseasonal precipitation anomalies vs. tropical mean tropospheric temperature, defined as the average in pressure coordinates from the surface to 100 hPa. Since all models are run over nearly identical fixed SSTs, the differences in the tropospheric temperatures in this figure come primarily from the upper troposphere. Figure 10 shows that the strength of ISV is linearly related to the tropical mean tropospheric temperature with a negative slope. Observations lie in the middle of the spread of the simulations. The CAM3.1R models have similar tropospheric temperature, as well as similar strength of ISV. With less convective rainfall fraction, one can expect that the diabatic heating in the upper troposphere is reduced. Reduced diabatic heating by convection results in a reduced temperature of the upper troposphere, destabilizing the atmospheric column. And, reduced cloud height with reduced fraction of convective rainfall enhances radiative cooling by decreasing greenhouse effect of high clouds. A full analysis of the tropical static stability in the strong-ISV and weak-ISV versions of the

SNU model, and its effect on the speed of convectively coupled Kelvin waves was performed in Frierson et al (2010).

Using a reduced-complexity model of the tropical atmosphere, Raymond (2001) suggested that the local relationship between moisture and precipitation is crucial for the MJO to be sustained. He showed that precipitation in his model, which simulates the MJO, is inversely proportional to saturation deficit. The relationship between column moisture and precipitation in satellite observations was investigated by Bretherton et al. (2004), who showed that, on monthly and daily time scales, the mean value of precipitation occurring at a given column relative humidity increases exponentially when the latter is larger than some critical value. Peters and Neelin (2006) and Neelin et al. (2009) examined the relationship more thoroughly. They found that the relationship between precipitable water and precipitation can be generalized when precipitable water is rescaled by critical precipitable water, which is a function of tropospheric temperature. It is reasonable to think that the observed moisture-precipitation relationship is one of characteristic features that should be simulated correctly to simulate other phenomena (e.g. the MJO) accurately, though a theory for such a linkage remains incomplete.

In recent studies, the local moisture-precipitation relationship has been suggested as a diagnostic tool to distinguish strong-MJO models from weak-MJO ones. The precipitation composite based on saturation fraction, which is used in Zhu

et al. (2009), and the composite of relative humidity against precipitation in Thayer-Calder and Randall (2009), were shown to be useful for this purpose. By comparing CAM3.0 and SPCAM, Zhu et al. (2009) and Thayer-Calder and Randall (2009) showed that accurately representing the relationship between column moisture and precipitation is necessary for a GCM to simulate the MJO properly.

Figure 11 shows the observed and simulated relative humidity composited based on precipitation for strong- and weak-ISV models. The x-axis of the plot is \log_{10} of precipitation in units of mm day^{-1} . Thayer-Calder and Randall (2009) showed that, in observations and a model which simulates the MJO well (SPCAM), there is a gradual moistening of the troposphere accompanied by a deepening of the high relative humidity area. In SNU and CAM3.1R, there is an increase of relative humidity in the mid- and lower troposphere at high rain rates in the strong-ISV version, while the relative humidity is decreased in the strong-ISV version of AM2. 75 percent contours are drawn to highlight the gradual deepening of the high relative humidity area. These have slopes more similar to that observed in the strong-ISV models than in the weak-ISV models. However, this diagnostic does not explain all the differences because, for example, the SNU model with minimum entrainment rate threshold 0.1 has stronger ISV and a higher east/west ratio than the AM2 model with threshold 0.025, although the slope of the 75 percent contour seems to be more similar to that observed in the AM2 model.

Similarly to Zhu et al. (2009), precipitation is composited based on saturation fraction over the warm pool region in Figure 12 (upper panels). In this diagram, we used the ERA-Interim data for temperature and the SSM/I-TMI combined data for precipitable water to calculate the saturation fraction. For precipitation, the GPCP product version 1.1 is used. In general, composited precipitation is near zero until the saturation fraction reaches some critical value, after which precipitation increases rapidly. When we compare weak-ISV models (dashed line) to strong-ISV models (solid line), however, the three sets of models show three distinct types of behavior in terms of the critical value and the slope of the curve for saturation fraction larger than that value. Here, the critical value is loosely defined as the point after which the slope of the curve increases significantly. In AM2, the slope from the strong-ISV version is steeper than that of the weak-ISV version, while both show similar critical values. The two versions of the SNU model have similar slopes and critical values. The critical value is significantly increased in CAM3.1R with larger convective rain re-evaporation efficiency. The different behavior of the relationships between moisture and precipitation are interesting because the convection schemes used in these three models are similar (Table 1).

The probability density function (PDF) of saturation fraction is also shown in Figure 12 (middle panel). In observations (black line), the peak of the PDF is near 0.8, after which the PDF drops quickly. The peaks of the PDF in the AM2 models are similar to the observed value, while the SNU models have peaks near 0.6. The two

different versions of CAM3.1R show quite different shapes of the PDF. The most frequent value of the saturation fraction moves from near 0.7 in weak-ISV version to about 0.9 in strong-ISV version. In all three models, the occurrence of high saturation fractions (right tail of the curve) increases. When the composited precipitation is weighted by the PDF of saturation fraction (Figure 8, lower panel), the difference between strong- and weak-ISV models becomes more similar among the three models. The PDF-weighted composited precipitation can be regarded as the expected value of the precipitation for a given saturation fraction value, the sum of which is the mean precipitation. The amount of precipitation that occurs at high saturation fraction increases with stronger ISV in all three models used in this study.

Considered together, the plots shown in figures 11 and 12 suggest that the joint relationship between humidity and precipitation needs not differ in a systematic way between strong- and weak-ISV models. This is somewhat contrary to expectations based, for example, on previous studies which have demonstrated some correspondence between the shape of the precipitation-saturation fraction curve and the simulation of ISV (e.g. Zhu et al. 2009).

4. Summary and conclusions

We used ten different AGCM simulations to investigate systematic relationships between ISV simulations and mean state bias. The ten models are clustered into two groups in terms of the strength of their ISV, which is defined as the area-averaged

standard deviation of ISV over the tropics.

The strong-ISV models have magnitudes of ISV stronger than those of the weak-ISV models and of observations (Fig. 3). The observed value is in between the two model groups. The eastward/westward ratio and variance of ISV are closely related in these models; the eastward/westward ratios of the strong-ISV models are larger than those of the weak-ISV models and closer to the observed value. However, observations deviate from the simulated relationship between these two ISV properties, having larger eastward/westward ratio for the same variance as in the simulations.

It is shown that the pattern of boreal summer/winter mean precipitation is closely related to the strength of ISV (Fig. 6). The strong-ISV models show a wet (dry) bias over the western Pacific (equatorial Indian Ocean) during boreal summer, while the signs of the biases are reversed in the weak-ISV models. Similarly, during boreal winter, the amount of simulated precipitation in the SPCZ (ITCZ) region is larger (smaller) in the strong-ISV models than in weak-ISV models.

Three sets of paired simulations (AM2, SNU, CAM3.1R), in which only one parameter in the convection scheme is changed to enhance the moisture sensitivity of convection, are used to find common differences between the two groups. The mean and variance of surface latent heat flux is increased in the strong-ISV versions, consistent with the hypothesis that wind-evaporation feedback is too strong in these

models. The annual mean convective rain fraction is reduced in the strong-ISV versions in all models, presumably as a direct result of the modifications implemented in the convective schemes to increase their sensitivity to environmental moisture. Relative humidity composites based on precipitation are also examined. Although strong-ISV versions tend to represent the gradual deepening of the high relative humidity layer as a function of precipitation better compared to weak-ISV versions, it is hard to explain the inter-model differences using this diagnostic. Differences between weak- and strong-ISV versions in the composited relationship between precipitation and saturation fraction are not consistent across the three model pairs. On the other hand, there is a consistent difference in the frequency distributions of the saturation fraction and precipitation. In strong-ISV models, high values of saturation fraction and precipitation occur more frequently and make a greater contribution to the total precipitation.

Previous studies have shown that the strength of ISV simulated by GCMs can be controlled through modifications to the convection scheme. When convection is made more sensitive to environmental moisture, ISV becomes stronger. This method is often used to improve a model's ability to represent the MJO, the dominant mode of ISV in the tropics. Recent intercomparison studies, however, have demonstrated that most GCMs involved in the 4th assessment report (AR4) of the Intergovernmental Panel on Climate Change (IPCC) have poor MJOs (Lin et al. 2006). The systematic relationships shown here between ISV characteristics and mean state

bias may partly explain the current situation in which poor-ISV models are used operationally even though modelers know how to improve ISV. Presumably, most important purpose of most operational climate models is long-term climate projection, for which a realistic mean climate is a higher priority than intraseasonal variability.

It is worthwhile to note that the models used in this study are atmosphere-only models, in which sea surface temperature is prescribed as a boundary condition. When sea surface temperature is prescribed into AGCMs, positive moisture-convection feedbacks over the warm pool produce excessive rainfall there. This is in part because of the lack of negative feedback mechanisms (e.g. reduced shortwave radiation and enhanced latent heat flux cooling down surface temperature) in the AGCMs. Stan et al. (2010) showed that excessive precipitation over the west Pacific during boreal summer disappears when the SPCAM is coupled to an ocean model, suggesting the possibility that the relationship examined here may not be expected to hold in coupled GCMs (though they might perhaps lead to ocean biases instead). The current study calls for examinations of relationship between ISV and mean state in ocean-atmosphere coupled models.

Acknowledgements

The ERA-interim data used in this study have been provided by ECMWF data server. We thank to Dr. Suzana Camargo for kindly providing scripts to generate SSM/I-TMI combined precipitable water data. This work was supported by NASA grant NNX09AK34G (DK, AHS) and NOAA grant NA08OAR4320912 (AHS, EDM, DMWF). This work was also supported by the Climate and Large-Scale Dynamics Program of the National Science Foundation under Grants ATM-0832868 and ATM-1025584 (EDM). ISK is supported by the Korea Meteorological Administration Research and Development Program under Grant CATER_2006-4206 and the second stage of the Brain Korea 21. DMWF is supported by NSF grants ATM-0846641 and ATM-0936059.

Reference

- Bergman, J. W., H. H. Hendon, and K. M. Weickmann, 2001: Intraseasonal Air-Sea Interactions at the Onset of El Niño. *Journal of Climate*, **14**, 1702-1719.
- Bessafi, M. and M. C. Wheeler, 2006: Modulation of South Indian Ocean Tropical Cyclones by the Madden-Julian Oscillation and Convectively Coupled Equatorial Waves. *Monthly Weather Review*, **134**, 638-656.
- Bretherton, C. S., M. E. Peters, L. E. Back, 2004: Relationships between Water Vapor Path and Precipitation over the Tropical Oceans. *J. Climate*, **17**, 1517-1528.
- Frierson, D. M. W., Kim, D., Kang, I.-S., Lee, M.-I., and J.-L. Lin, 2010: Structure of AGCM-Simulated Convectively Coupled Equatorial Waves and Sensitivity to Convective Parameterization. *J. Atmos. Sci.*, in press.
- Hannah, W. M., and E. D. Maloney, 2010: The role of moisture-convection feedbacks in simulating the Madden-Julian oscillation. *J. Climate*, accepted pending revisions.
- Huffman, G. J., R. F. Adler, M. M. Morrissey, D. T. Bolvin, S. Curtis, R. Joyce, B. McGavock, and J. Susskind, 2001: Global precipitation at one-degree daily resolution from multisatellite observations. *Journal of Hydrometeorology*, **2**, 36-50.
- Kalnay, E., M. Kanamitsu, R. Kistler, W. Collins, D. Deaven, L. Gandin, M. Iredell, S. Saha, G. White, J. Woollen, Y. Zhu, M. Chelliah, W. Ebisuzaki, W. Higgins, J. Janowiak, K. C. Mo, C. Ropelewski, J. Wang, A. Leetmaa, R. Reynolds, R. Jenne, and D. Joseph, 1996: The NCEP/NCAR 40-year reanalysis project. *Bulletin of the American Meteorological Society*, **77**, 437-471.
- Kessler, W. S., 2001: EOF representations of the Madden-Julian oscillation and its connection with ENSO. *Journal of Climate*, **14**, 3055-3061.
- Khairoutdinov, M. and D. Randall, 2001: A cloud resolving model as a cloud parameterization in the NCAR Community Climate System Model: Preliminary results. *Geophys. Res. Lett.*, **28**, 3617-3620.
- Khairoutdinov, M., D. Randall, and C. DeMott, 2005: Simulations of the Atmospheric General Circulation Using a Cloud-Resolving Model as a Superparameterization of Physical Processes. *Journal of the Atmospheric Sciences*, **62**, 2136-2154.
- Lee, M. I., I. S. Kang, and B. E. Mapes, 2003: Impacts of cumulus convection parameterization on aqua-planet AGCM Simulations of tropical intraseasonal variability. *Journal of the Meteorological Society of Japan*, **81**, 963-992.
- Lee, M. I., I. S. Kang, J. K. Kim, and B. E. Mapes, 2001: Influence of cloud-radiation interaction on simulating tropical intraseasonal oscillation with an atmospheric general circulation model. *Journal of Geophysical Research-Atmospheres*, **106**, 14219-14233.
- Liebmann, B., H. H. Hendon, and J. D. Glick, 1994: The relationship between tropical cyclones of the western Pacific and Indian Oceans and the Madden-Julian oscillation. *J. Meteor. Soc. Japan*, **72**, 401-411.
- Lin, J. L., M. I. Lee, D. Kim, I. S. Kang, and D. M. W. Frierson, 2008: The Impacts of

- Convective Parameterization and Moisture Triggering on AGCM-Simulated Convectively Coupled Equatorial Waves. *Journal of Climate*, **21**, 883-909.
- Lin, J. L., G.N. Kiladis, B.E. Mapes, K.M. Weickmann, K.R. Sperber, W.Y. Lin, M. Wheeler, S.D. Schubert, A. Del Genio, L.J. Donner, S. Emori, J.-F. Gueremy, F. Hourdin, P.J. Rasch, E. Roeckner, and J. F. Scinocca, 2006: Tropical intraseasonal variability in 14 IPCC AR4 climate models. Part I: Convective signals. *Journal of Climate*, **19**, 2665–2690.
- Luo, Z. and G. Stephens, 2006: An enhanced convection-wind-evaporation feedback in a superparameterization GCM (SP-GCM) depiction of the Asian summer monsoon. *Geophys. Res. Lett*, **33**, L06707.
- Madden, R. A. and P. R. Julian, 1971: Detection of a 40-50 day oscillation in the zonal wind in the tropical Pacific. *J. Atmos. Sci.*, **28**, 702-708.
- —, 1972: Description of Global-Scale Circulation Cells in the Tropics with a 40-50 Day Period. *Journal of the Atmospheric Sciences*, **29**, 1109-1123.
- Maloney, E. D. and D. L. Hartmann, 2000a: Modulation of hurricane activity in the Gulf of Mexico by the Madden-Julian oscillation. *Science*, **287**, 2002-2004.
- —, 2000b: Modulation of eastern North Pacific hurricanes by the Madden-Julian oscillation. *Journal of Climate*, **13**, 1451-1460.
- —, 2001: The sensitivity of intraseasonal variability in the NCAR CCM3 to changes in convective parameterization. *Journal of Climate*, **14**, 2015-2034.
- Maloney and Sobel 2004: Surface fluxes and ocean coupling in the tropical intraseasonal oscillation. *Journal of Climate*, **17**, 4368-4386.
- Maloney, Sobel, and Hannah 2010: Intraseasonal variability in an aquaplanet general circulation model. *Journal of Advances in Modeling Earth Systems*, **2**, doi:10.3894/JAMES.2010.2.5.
- Moorthi, S. and M. J. Suarez, 1992: Relaxed Arakawa-Schubert. A parameterization of moist convection for general circulation models. *Monthly Weather Review*, **120**, 978-1002.
- Neale, R. B., J. H. Richter, and M. Jochum, 2008: The impact of convection on ENSO: From a delayed oscillator to a series of events. *Journal of Climate*, **21**, 5904-5924.
- Neelin, J. D., O. Peters, K. Hales, 2009: The Transition to Strong Convection. *J. Atmos. Sci.*, **66**, 2367–2384.
- Numaguti, A., M. Takahashi, T. Nakajima, and A. Sumi, 1995: Development of an atmospheric general circulation model. *Climate System Dynamics and Modeling*, **3**, 1-27.
- Peters, O., and J. D. Neelin, 2006: Critical phenomena in atmospheric precipitation. *Nature Phys.*, **2**, 393–396, doi:10.1038/nphys314.
- Raymond, D. J., 2001: A New Model of the Madden-Julian Oscillation. *J. Atmos. Sci.*, **58**, 2807–2819.
- Simmons, A. and coauthors., 2007: ERA-Interim: New ECMWF reanalysis products from 1989 onwards. *ECMWF Newsletter*, **110**, 25-35.
- Slingo, J. M., K. R. Sperber, J. S. Boyle, J. P. Ceron, M. Dix, B. Dugas, W. Ebisuzaki, J.

- Fyfe, D. Gregory, J. F. Gueremy, J. Hack, A. Harzallah, P. Inness, A. Kitoh, W. K. M. Lau, B. McAvaney, R. Madden, A. Matthews, T. N. Palmer, C. K. Park, D. Randall, and N. Renno, 1996: Intraseasonal oscillations in 15 atmospheric general circulation models: Results from an AMIP diagnostic subproject. *Climate Dynamics*, **12**, 325-357.
- Sobel, A., E. Maloney, G. Bellon, and D. Frierson, 2010: Surface fluxes and tropical intraseasonal variability: a reassessment. *J. Adv. Model. Earth Syst*, **2** doi:10.3894/JAMES.2010.2.2.
- Takayabu, Y. N., T. Iguchi, M. Kachi, A. Shibata, and H. Kanzawa, 1999: Abrupt termination of the 1997-98 El Nino in response to a Madden-Julian oscillation. *Nature*, **402**, 279-282.
- Thayer-Calder, K. and D. Randall, 2009: The role of convective moistening in the Madden-Julian Oscillation. *Journal of the Atmospheric Sciences*, **66**, 3297-3312.
- Tokioka, T., K. Yamazaki, A. Kitoh, and T. Ose, 1988: The equatorial 30-60 day oscillation and the Arakawa-Schubert penetrative cumulus parameterization. *Journal of the Meteorological Society of Japan*, **66**, 883-901.
- Wang, W. Q. and M. E. Schlesinger, 1999: The dependence on convection parameterization of the tropical intraseasonal oscillation simulated by the UIUC 11-layer atmospheric GCM. *Journal of Climate*, **12**, 1423-1457.
- Wheeler, M., and G. N. Kiladis, 1999: Convectively coupled equatorial waves: Analysis of clouds and temperature in the wavenumber-frequency domain. *J. Atmos. Sci.*, **56**, 374-399.
- Wheeler, M. C. and J. L. McBride, 2005: Australian-Indonesian monsoon. *Intraseasonal Variability in the Atmosphere-Ocean Climate System*, W. K. M. Lau and D. E. Waliser, Eds., Springer, Heidelberg, Germany, 125-173.
- Yasunari, T., 1979: Cloudiness fluctuations associated with the Northern Hemisphere summer monsoon. *J. Met. Soc. Japan*, **57**, 227-242.
- Zhang, G. and N. McFarlane, 1995: Sensitivity of climate simulations to the parameterization of cumulus convection in the Canadian Climate Centre general circulation model. *Atmosphere Ocean*, **33**, 407-407.
- Zhang, G. J. and M. Mu, 2005: Simulation of the Madden-Julian Oscillation in the NCAR CCM3 Using a Revised Zhang-McFarlane Convection Parameterization Scheme. *Journal of Climate*, **18**, 4046-4064.
- Zhu, H., H. Hendon, and C. Jakob, 2009: Convection in a Parameterized and Superparameterized Model and Its Role in the Representation of the MJO. *Journal of the Atmospheric Sciences*, **66**, 2796-2811.

Table list

Table 1. Description of participating models

Figure list

Figure 1. All season standard deviation of 20-100 day band pass filtered precipitation. a) GPCP, b) AM2 (tok=0.025), c) SNU (tok=0.0), d) CAM3.1R (evap=0.05), e) CAM3.0+NRJ08, f) GEOS5, g) AM2 (tok=0.1), h) SNU (tok=0.1), i) CAM3.1R (evap=0.6), j) CAM3.0+ZM05, and k) CAM3.0+SP. The unit is $\text{mm}^2 \text{day}^{-2}$.

Figure 2. November-April lag-longitude diagram of 10°N - 10°S averaged intraseasonal 850 hPa zonal wind anomalies correlated against intraseasonal zonal wind anomalies at the Indian Ocean (70 - 95°E , 5°S - 5°N averaged) reference point. a) NCEP/NCAR, b) AM2 (tok=0.025), c) SNU (tok=0.0), d) CAM3.1R (evap=0.05), e) CAM3.0+NRJ08, f) GEOS5, g) ERAinterim, h) AM2 (tok=0.1), i) SNU (tok=0.1), j) CAM3.1R (evap=0.6), k) CAM3.0+ZM05, and l) CAM3.0+SP.

Figure 3. Scatter plot of standard deviation averaged over 0 - 360°E , 30°S - 30°N and east/west ratio, defined as ratio of eastward propagating spectral power (summation over wavenumber 1-3, period 30-70 day) to that of westward propagating counterpart. Open (close) circle represents weak (strong) ISV model.

Figure 4. Same as Figure 1, except for May-October mean precipitation. Unit is mm day^{-1} .

Figure 5. Same as Figure 4, except for November-April mean precipitation.

Figure 6. Scatter plots of standard deviation averaged over 0 - 360°E , 30°S - 30°N and a) May-October mean precipitation index which is defined as averaged precipitation over WP1 (120 - 160°E , 5°S - 20°N) minus IO (60 - 95°E , 15°S - 5°N), and b) November-April mean precipitation index defined as averaged precipitation over WP2 (140 - 180°E , 20°S -Eq.) minus EP (200 - 260°E , Eq.- 10°N). Open (close) circle represents weak (strong) ISV model.

Figure 7. Difference map of May-October precipitation (mm/day) a) AM2, b) SNU, and c) CAM3.1R. Difference map of May-October evaporation (W/m^2) e) AM2, f) SNU, and g) CAM3.1R.

Figure 8. Difference map of May-October standard deviation of 20-100 day filtered evaporation a) AM2, b) SNU, and c) CAM3.1R

Figure 9. Difference map of annual mean convective rain fraction a) AM2, b) SNU, and c) CAM3.1R

Figure 10. Scatter plots of standard deviation averaged over 0 - 360°E , 30°S - 30°N and mean tropospheric temperature averaged over 0 - 360°E , 30°S - 30°N . Open (close) circle

represents weak (strong) ISV model.

Figure 11. Composite vertical profile of relative humidity based on precipitation rate a) GPCP/ERAinterim, b) AM2 (Tok=0.025), c) AM2 (Tok=0.1), e) SNU (Tok=0.0), f) SNU (Tok=0.1), h) CAM3.1R (evap=0.05), and i) CAM3.1R (evap=0.6). Difference between strong- and weak-ISV models are shown in d) AM2, g) SNU, and j) CAM3.1R. The precipitation rate is plotted on a log scale with the relative humidity averaged for each bin shown on the x-axis. The data is analyzed over 40-180°E, 20°S.-20°N.

Figure 12. Upper: precipitation composite based on saturation fraction. Middle: probability density function (PDF) of saturation fraction, Lower: PDF weighted precipitation. Points over the west Pacific (130-180E, Eq.-20N) are used in calculations.

Table 1. Description of participating models

Model	Convection scheme	Version	Resolution	Period
AM2	RAS	tok=0.025 / 0.1	2.0°lat x 2.0°lon /L24	10yr with climatological SST
SNU	sRAS	tok=0.0 / 0.1	T42 /L20	20yr 01Jan1986- 31Dec2005
CAM3.1R	RAS	evap=0.05 / 0.6	T42 /L26	10yr with climatological SST
CAM3.0	ZM	Neale et al. (2008)	1.9°lat x 2.5°lon /L26	20yr 01Jan1986- 31Dec2005
		Zhang and Mu (2005)	T42 /L26	15yr 29Jan1980- 23Jul1995
	SP	Khairoutdinov et al. (2005)	T42 /L26	19 yr 1Oct1985- 25Sec2005
GEOS5	RAS	Rienecker et al. (2008) tok=0.05	1°lat x 1.25°lon /L72	12yr 1Dec1993- 30Nov2005

*RAS: Relaxed Arakawa-Schubert (Moorthi and Suarez 1992)

*sRAS: Simplified RAS (Numaguti et al. 1995)

*ZM: Zhang and McFarlane (1995)

*SP: Superparameterization (Khairoutdinov and Randall 2001)

*tok: constant in Tokioka modification (Tokioka et al. 1988)

*evap: rain re-evaporation constant in RAS

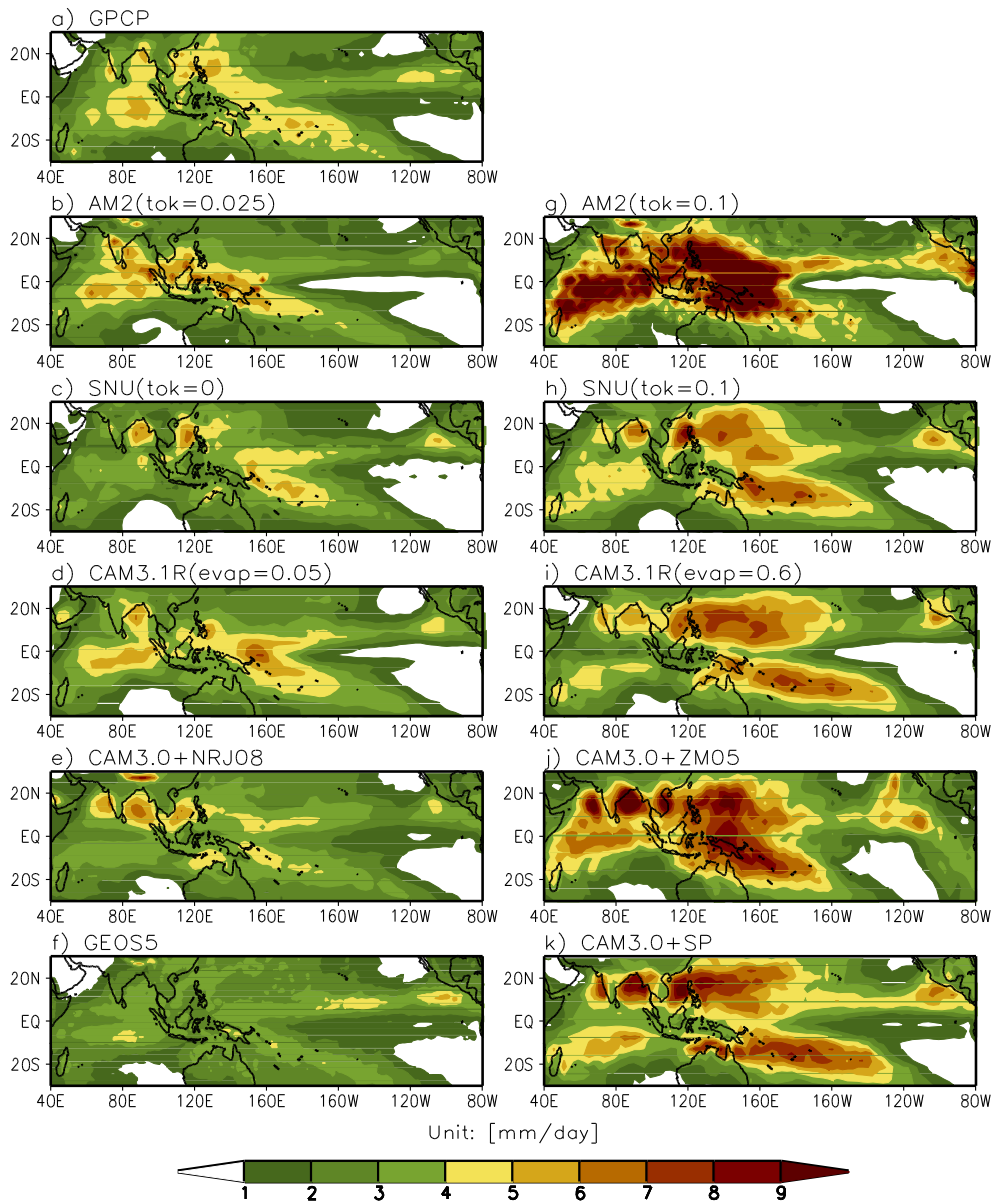


Figure 1. All season standard deviation of 20-100 day band pass filtered precipitation. a) GPCP, b) AM2 (tok=0.025), c) SNU (tok=0.0), d) CAM3.1R (evap=0.05), e) CAM3.0+NRJ08, f) GEOS5, g) AM2 (tok=0.1), h) SNU (tok=0.1), i) CAM3.1R (evap=0.6), j) CAM3.0+ZM05, and k) CAM3.0+SP. The unit is $\text{mm}^2 \text{day}^{-2}$.

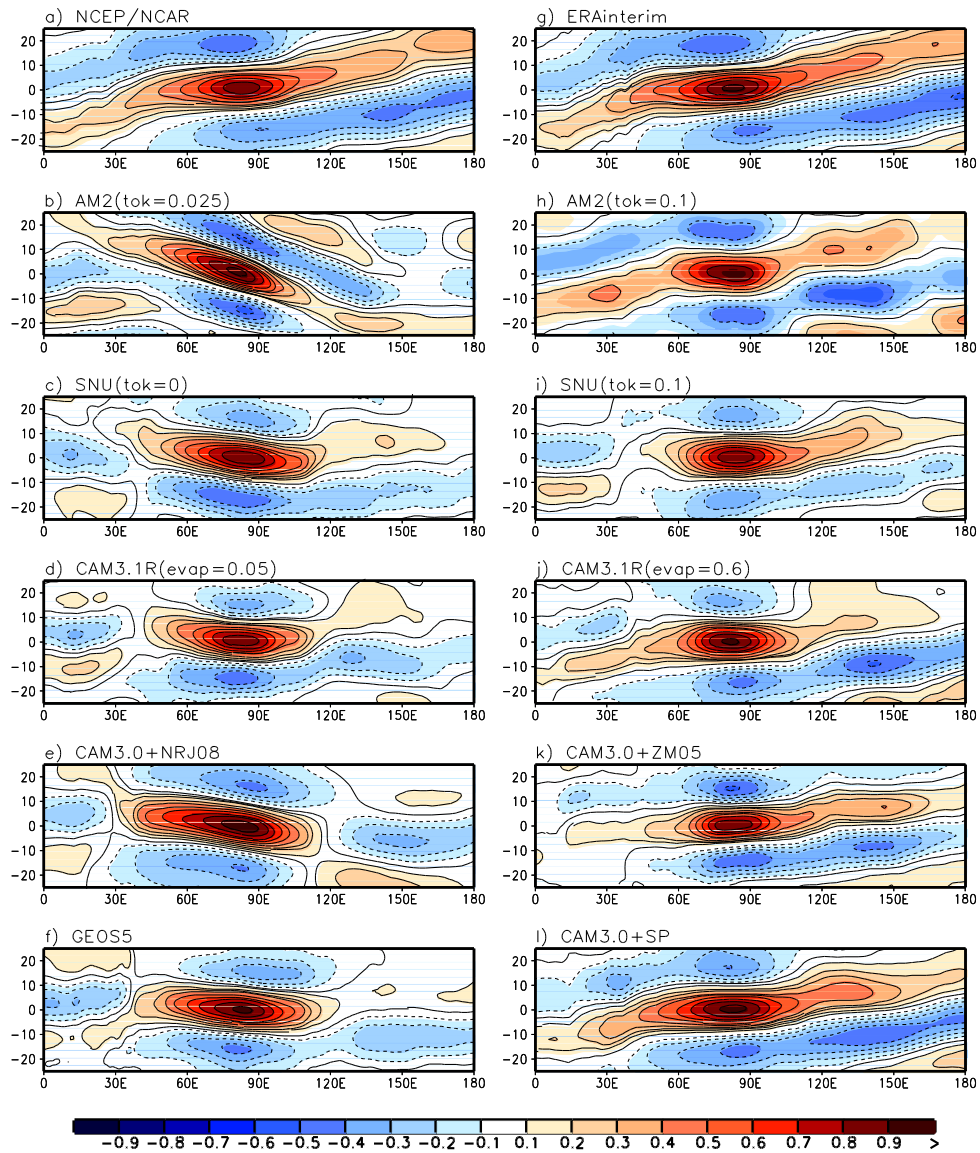


Figure 2. November-April lag-longitude diagram of 10°N - 10°S averaged intraseasonal 850 hPa zonal wind anomalies correlated against intraseasonal zonal wind anomalies at the Indian Ocean (70 - 95°E , 5°S - 5°N averaged) reference point. a) NCEP/NCAR, b) AM2 (tok=0.025), c) SNU (tok=0.0), d) CAM3.1R (evap=0.05), e) CAM3.0+NRJ08, f) GEOS5, g) ERAinterim, h) AM2 (tok=0.1), i) SNU (tok=0.1), j) CAM3.1R (evap=0.6), k) CAM3.0+ZM05, and l) CAM3.0+SP.

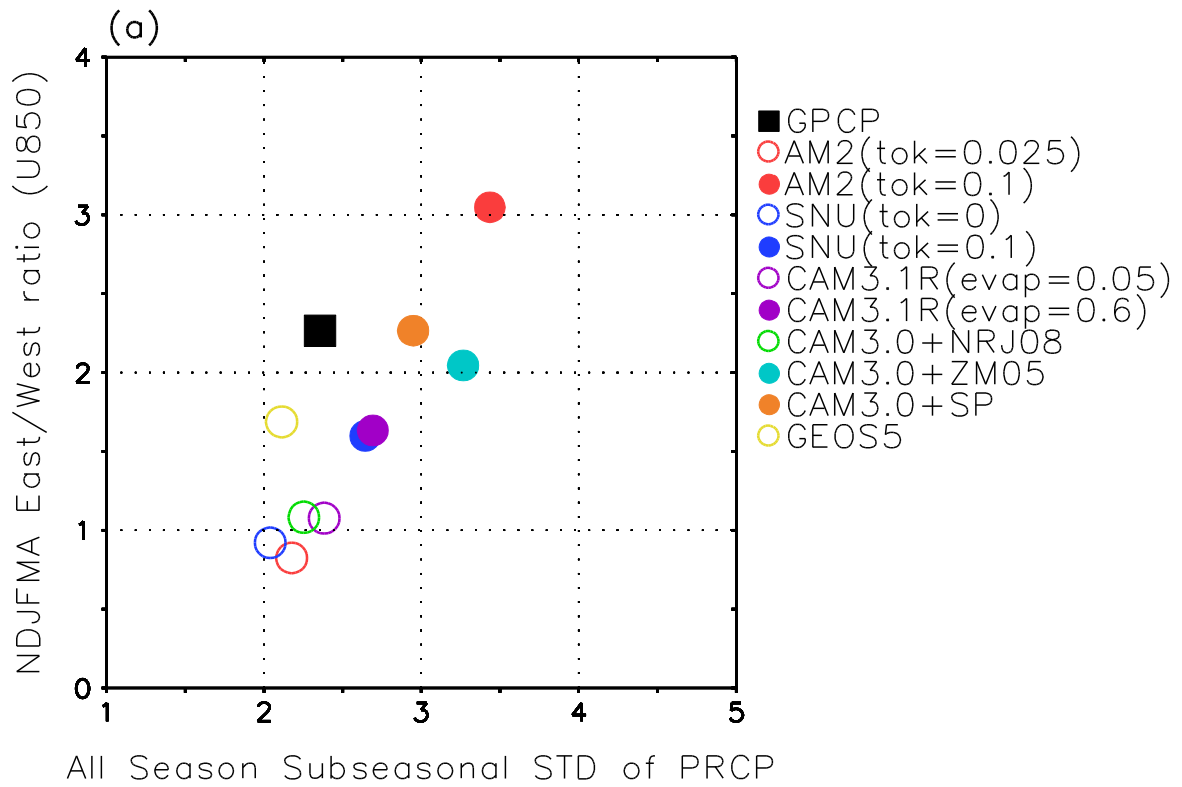


Figure 3. Scatter plot of standard deviation averaged over 0-360°E, 30°S-30°N and east/west ratio, defined as ratio of eastward propagating spectral power (summation over wavenumber 1-3, period 30-70 day) to that of westward propagating counterpart. Open (close) circle represents weak (strong) ISV model.

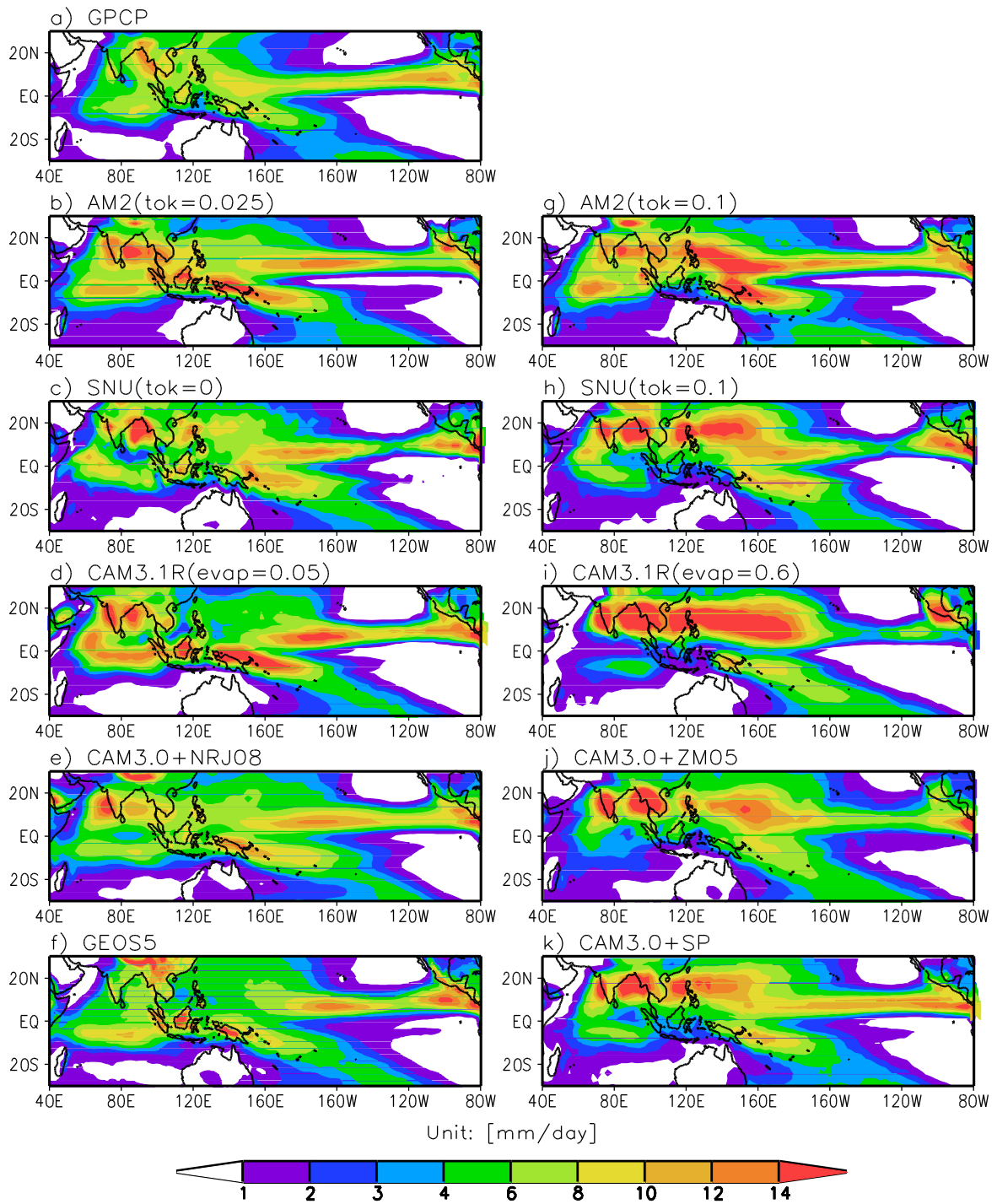


Figure 4. Same as Figure 1, except for May-October mean precipitation. Unit is mm day⁻¹.

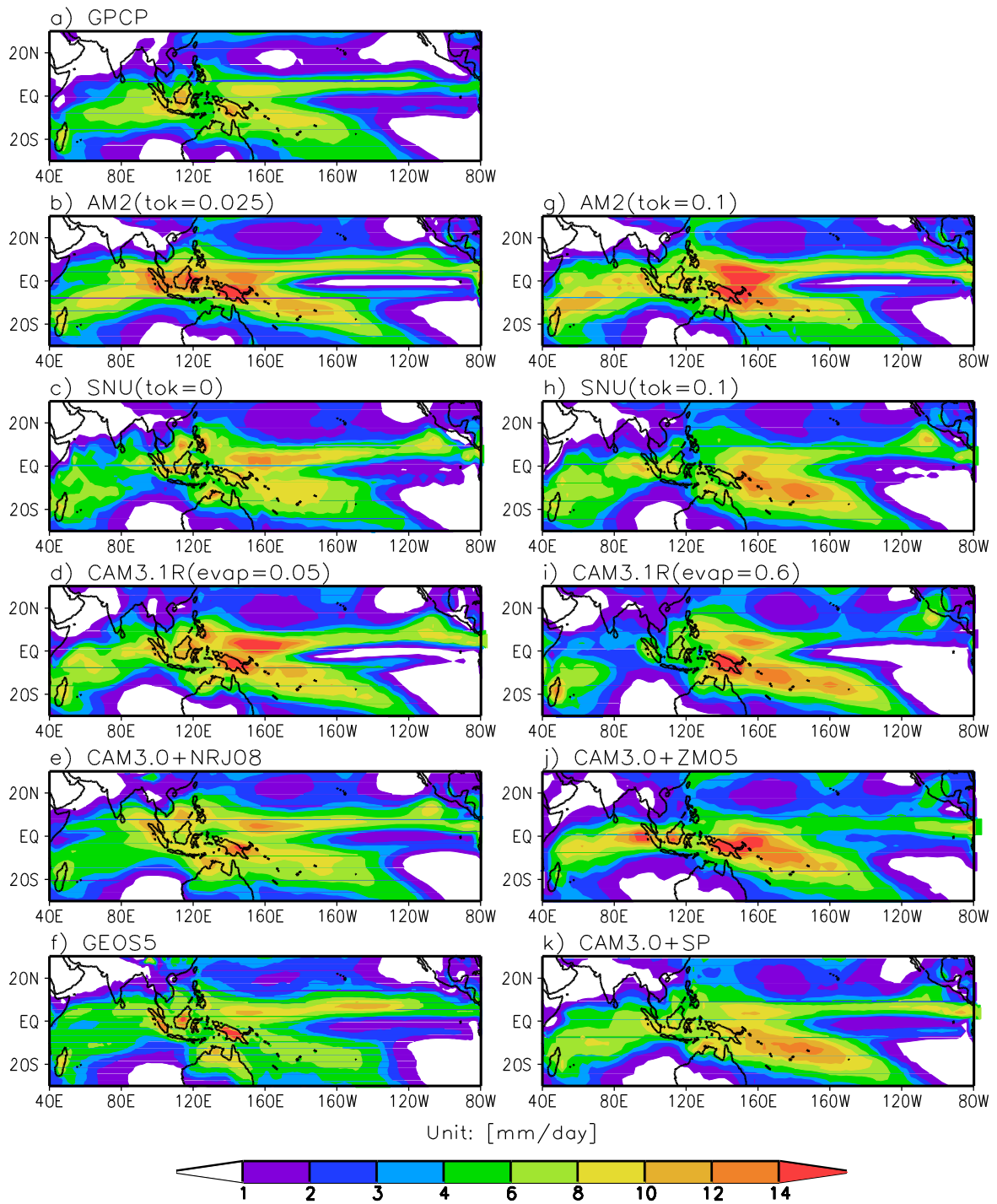


Figure 5. Same as Figure 4, except for November-April mean precipitation.

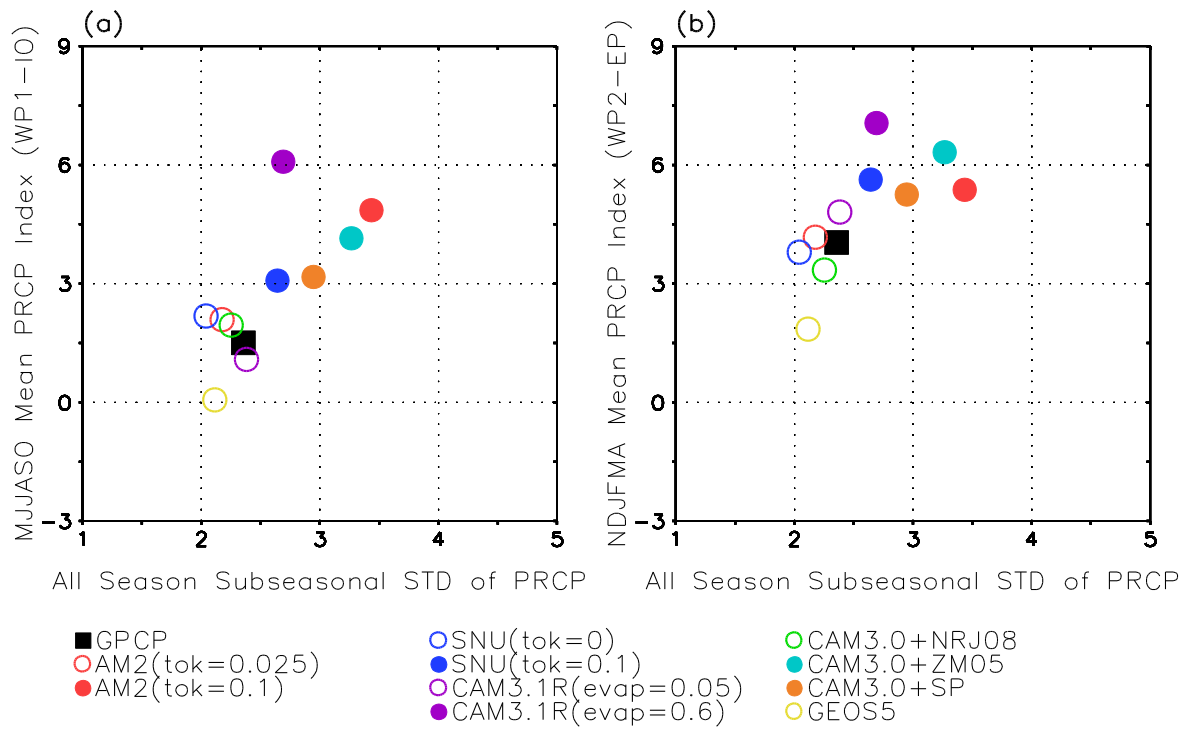


Figure 6. Scatter plots of standard deviation averaged over 0-360°E, 30°S-30°N and a) May-October mean precipitation index which is defined as averaged precipitation over WP1 (120-160°E, 5°S-20°N) minus IO (60-95°E, 15°S-5°N), and b) November-April mean precipitation index defined as averaged precipitation over WP2 (140-180°E, 20°S-Eq.) minus EP (200-260°E, Eq.-10°N). Open (close) circle represents weak (strong) ISV model.

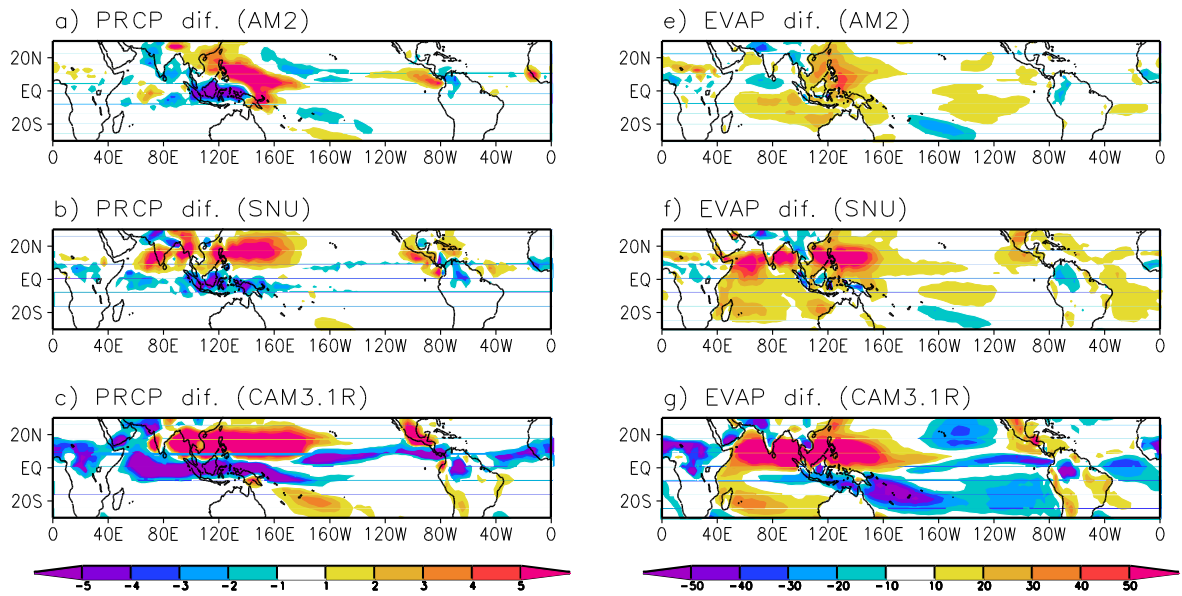


Figure 7. Difference map of May-October precipitation a) AM2, b) SNU, and c) CAM3.1R. Difference map of May-October evaporation e) AM2, f) SNU, and g) CAM3.1R.

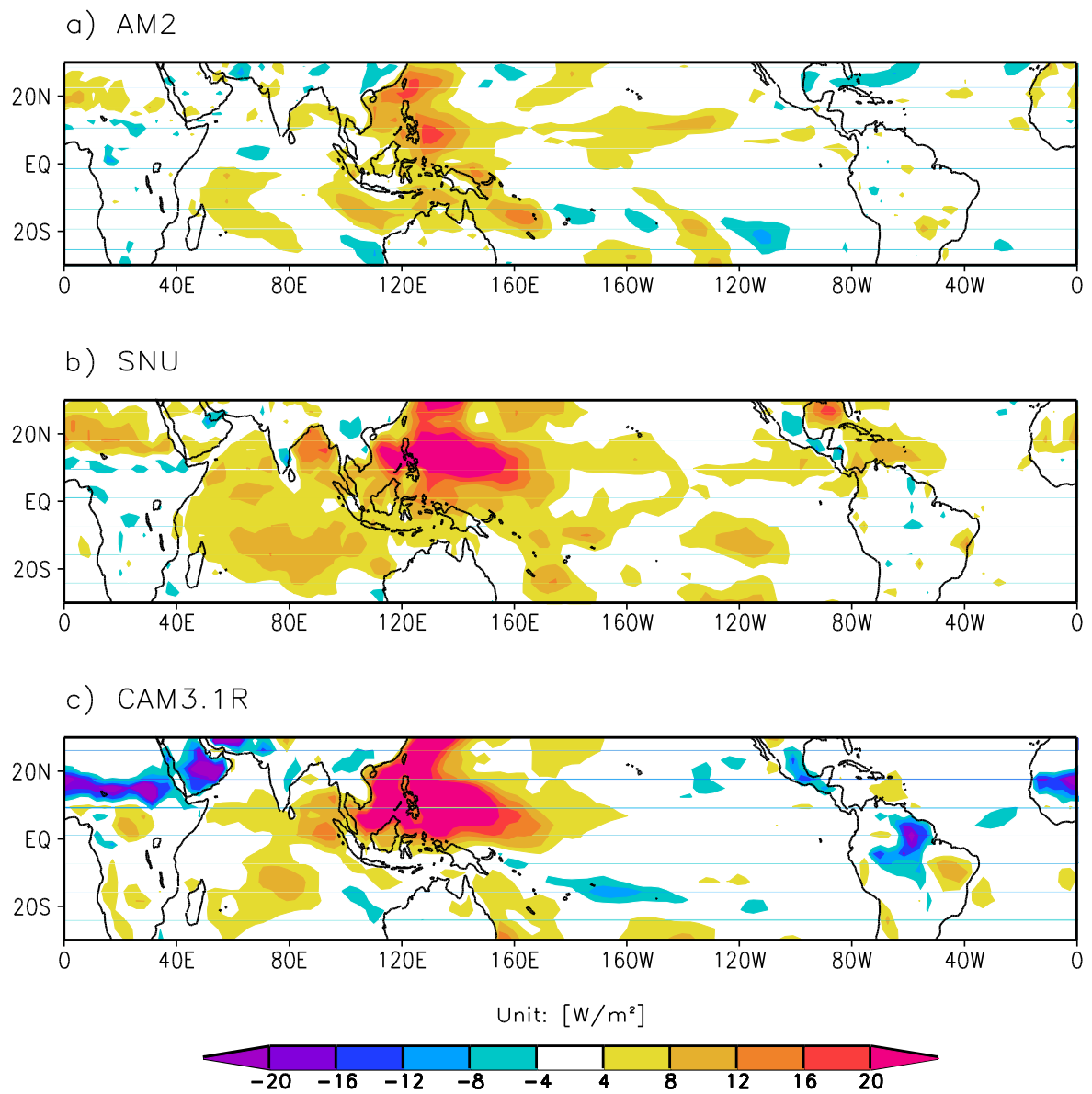


Figure 8. Difference map of May-October standard deviation of 20-100 day filtered evaporation a) AM2, b) SNU, and c) CAM3.1R

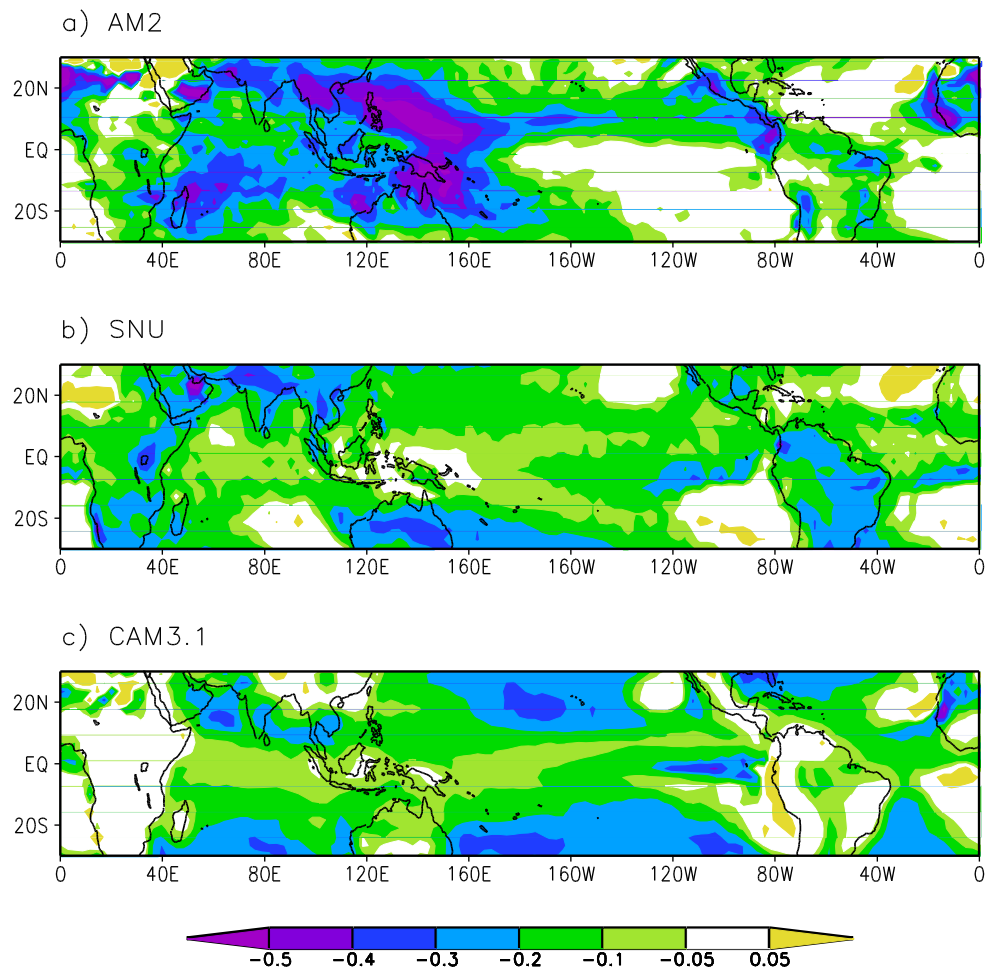


Figure 9. Difference map of annual mean convective rain fraction a) AM2, b) SNU, and c) CAM3.1R

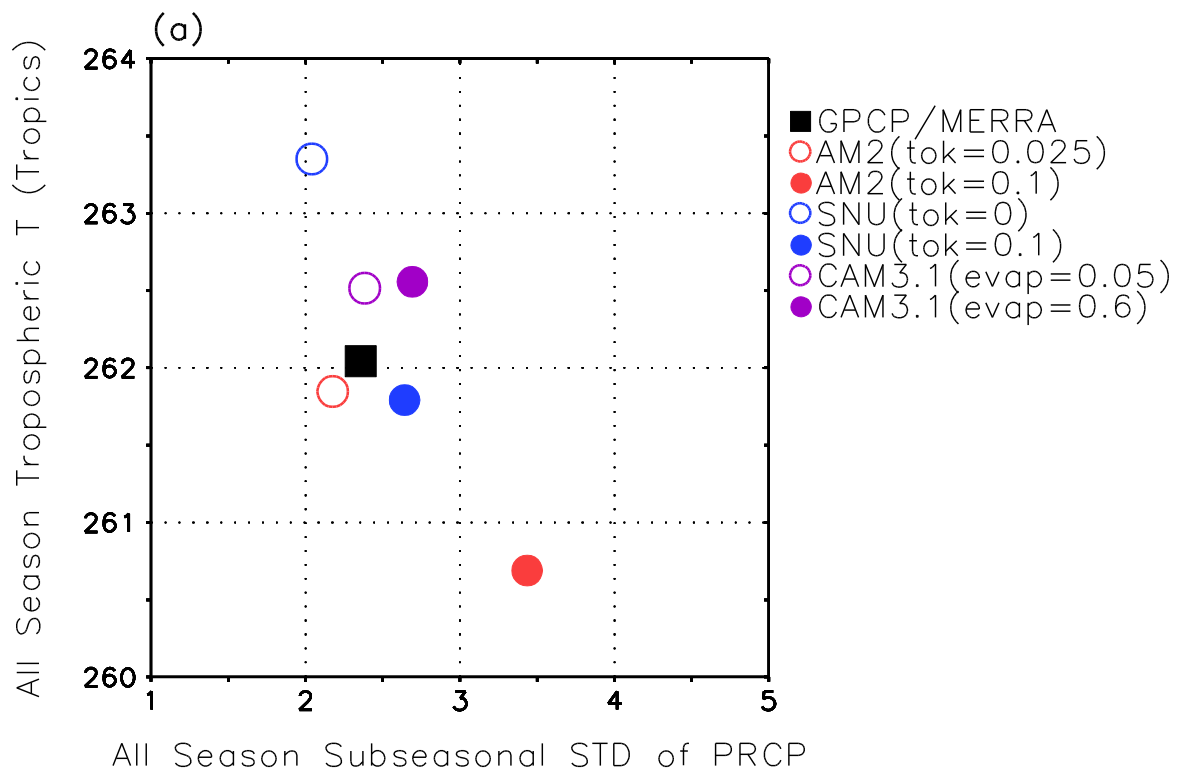


Figure 10. Scatter plots of standard deviation averaged over 0-360°E, 30°S-30°N and mean tropospheric temperature averaged over 0-360°E, 30°S-30°N. Open (close) circle represents weak (strong) ISV model.

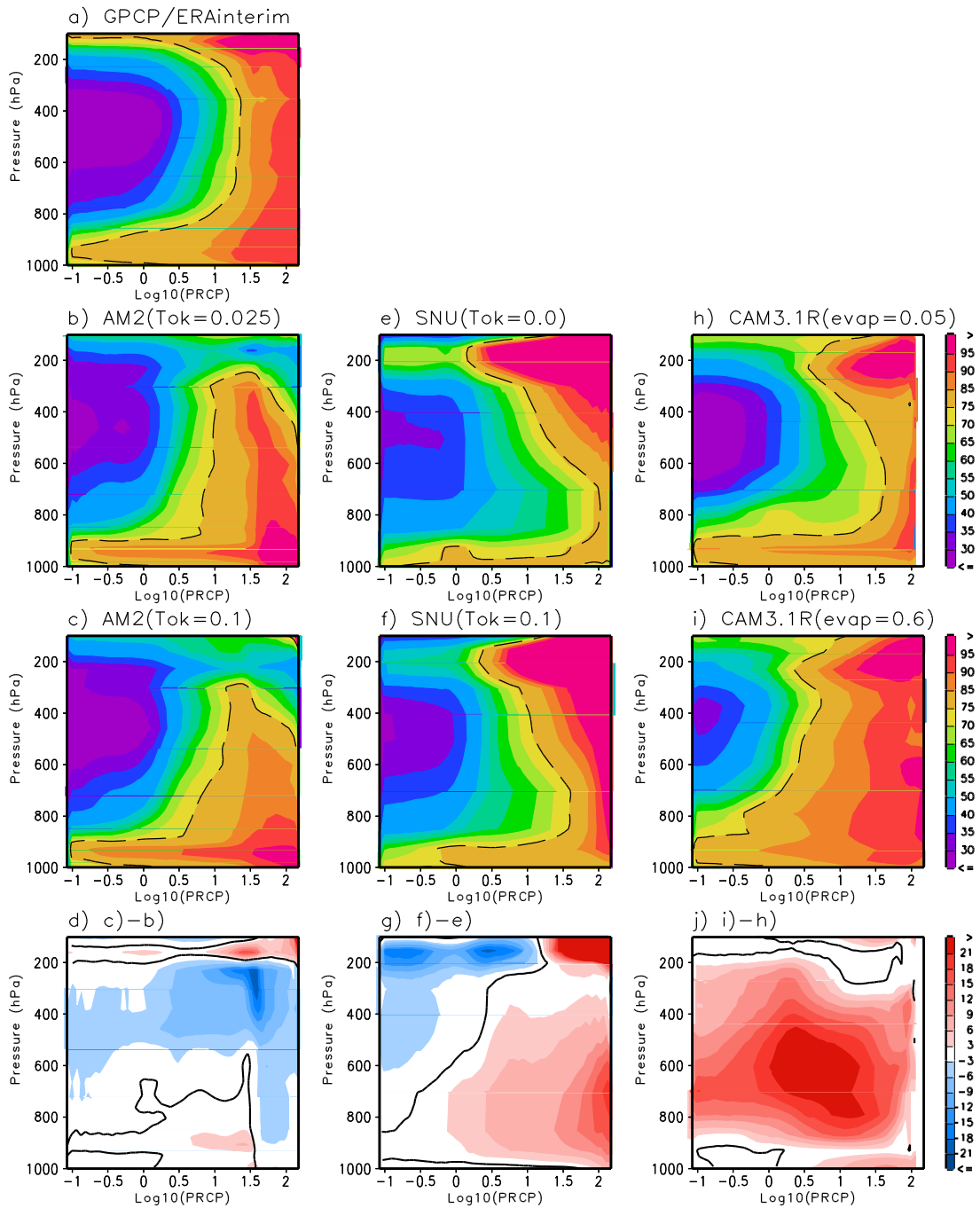


Figure 11. Composite vertical profile of relative humidity based on precipitation rate a) GPCP/ERAinterim, b) AM2 (Tok=0.025), c) AM2 (Tok=0.1), e) SNU (Tok=0.0), f) SNU (Tok=0.1), h) CAM3.1R (evap=0.05), and i) CAM3.1R (evap=0.6). Difference between strong- and weak-ISV models are shown in d) AM2, g) SNU, and j) CAM3.1R. The precipitation rate is plotted on a log scale with the relative humidity averaged for each bin shown on the x-axis. The data is analyzed over 40-180°E, 20°S-20°N.

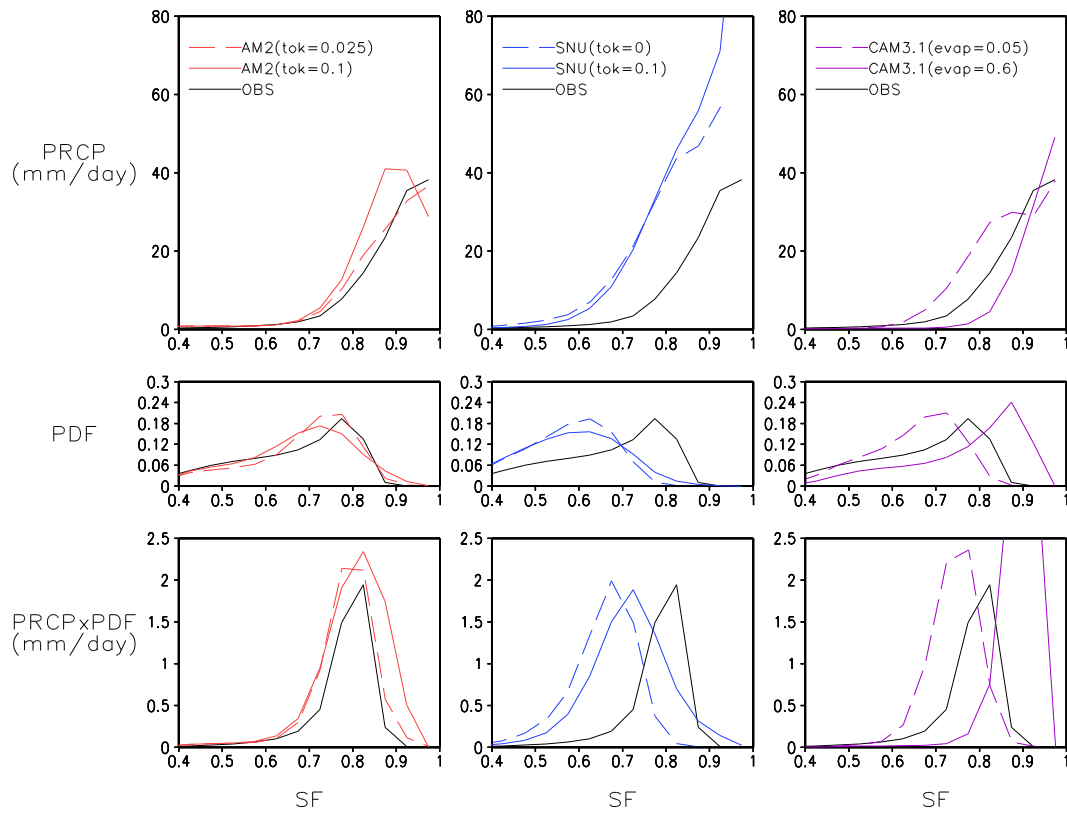


Figure 12. Upper: precipitation composite based on saturation fraction. Middle: probability density function (PDF) of saturation fraction, Lower: PDF weighted precipitation. Points over the warm pool region (40-180°E, 20°S-20°N) are used in calculations.